Increasing the speed of automated ultrasonic inspection of as-built additive manufacturing components by the adoption of virtual source aperture

Rastislav Zimermann [a,*], Ehsan Mohseni [a], Randika K.W. Vithanage [a], David Lines [a], Euan Foster [a], Charles N. Macleod [a], Stephen Gareth Pierce [a], Gianrocco Marinelli [b], Stewart Williams [b], Jialuo Ding [b]

[a] Centre for Ultrasonic Engineering, University of Strathclyde, Glasgow G1 1XW, UK
[b] Welding Engineering and Laser Processing Centre, University of Cranfield, Cranfield MK43 0AL, UK

HIGHLIGHTS

- Multi-layer adaptive ultrasound imaging using VSA for dry-coupled roller-probe inspection of AM components.
- Inspection of as-built dry-coupled Titanium WAAM components with artificial calibration reflectors.
- Increased data acquisition rate, increased speed of inspection and reduced data size while maintained sufficient SNR.

GRAPHICAL ABSTRACT
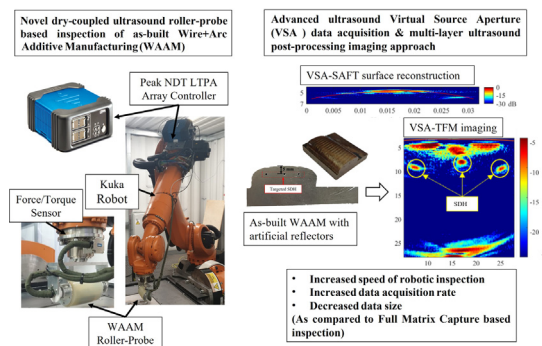
ARTICLE INFO

ABSTRACT

Wire + Arc Additive Manufacture (WAAM) is an economical manufacturing technique to build components. To maintain the commercial and technical benefits, inspection is desired at each layer of the build. New conformable phased array roller-probes offer the potential to inspect the as-built sample in-process or on completion.

A challenge with such inspections is the refraction of the ultrasonic waves at multiple interfaces. The Synthetic Aperture Focusing Technique (SAFT) and Total Focusing Method (TFM), combined with Full Matrix Capture (FMC) acquisition enabled imaging through the as-built WAAM surface. However, single-element firings, associated with FMC are a limiting factor due to the lower energy at transmission, while the high number of firings and subsequent larger data size negatively affect inspection speed.

This work introduces the concept of Virtual Source Aperture (VSA) for ultrasonic roller-probe inspection, through modelling of VSA on custom-designed calibration WAAM block. The concept is then demonstrated on a mock as-built WAAM sample inspection with reference defects. The results demonstrate that a markedly lower number of transmissions are required to match the performance of the FMC counterpart while increasing the energy levels. Moreover, an almost 50% reduction in the data size enabled a doubling of the inspection speed.

* Corresponding author at: Centre for Ultrasonic Engineering, University of Strathclyde, Glasgow G1 1XW, UK.
E-mail address: rastislav.zimermann@strath.ac.uk (R. Zimermann).

1. Introduction

Wire + Arc Additive Manufacturing (WAAM) is a directed energy deposition (ded) process [1], gaining popularity in the production of large complex metal components as seen in Fig. 1. Industrial robotic manipulators control arc-based deposition torches to lay the molten metal onto a substrate to achieve a pre-defined shape and height of a component. WAAM technology manifests its strengths of cost-effectiveness compared to subtractive machining from solid by achieving a significantly reduced waste of excess material and increasing time efficiency while manufacturing complex structures eliminating the need for assembly [2].

While the process is capable of manufacturing parts without any structural defects [4], flaws such as inclusion, porosity, and lack of fusion defects may be created because of poor process parameters or contaminated wire feedstock, which can impair the structural integrity of the component [5]. Delamination defects can be caused by insufficient remelting of the solids between layers. Cracks can also be created within the WAAM component, either by unfavourable solidification conditions or at grain boundaries due to morphology differences [6].

Therefore, such defects should be detected through post-deposition Non-Destructive Evaluation (NDE) inspections to ensure the quality and fitness of the components for their intended application.

NDE is frequently deployed for quality assessment and material characterization of manufactured components, without affecting their usability. The most common techniques employed for subsurface defect detection in additively manufactured metallic components include ultrasound [7], X-Ray computed tomography [8], eddy current [9], and thermography [10].

The sensitivity of ultrasonic testing to a range of defects of different shapes and sizes and its high-resolution imaging capabilities have made it the preferred technique for NDE of welding [11] and more recently additive manufacturing, especially WAAM [12–14]. The ultrasound wave is traditionally transmitted into the component using a piezoelectric single element transducer [15] in direct contact with the specimen and more recently through an ultrasound array [16], which features multiple piezoelectric elements within a common housing. These Phased Array Ultrasound Testing (PAUT) setups enabled volumetric imaging where the results can be presented in two/three-dimensional images/models, while also reducing the inspection time and increasing detection sensitivity
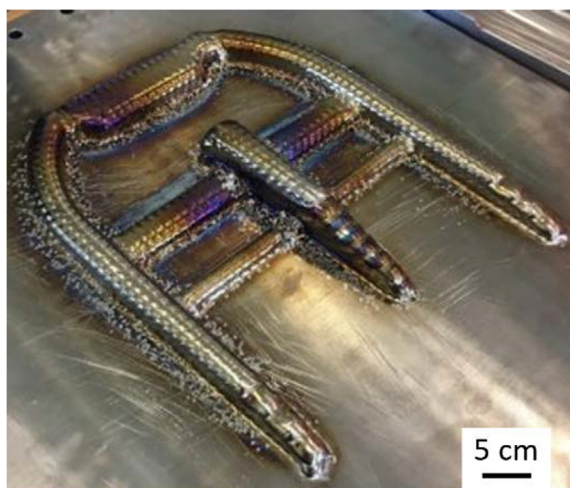
and accuracy [17]. Furthermore, differential time-delays between the excitation of individual elements of PAUT probes are used to steer and focus the beams into the desired locations where direct contact is not possible [18].

There has been a growing interest among different industrial sectors for incorporating automated NDE within their manufacturing [19], and some promising novel solutions have emerged through research and development for automated in-process PAUT inspection of welds [20–23] to meet such demands. These approaches are equally applicable for in-process inspection of WAAM to integrate the NDE within the manufacturing process, and hence, to gain evident benefits through cost-saving and increased throughput.

For robotic deployment of an ultrasound sensor over a hot as-built WAAM component, a novel dry-coupled high-temperature ultrasound phased array roller-probe, depicted in Fig. 2, has been developed [24]. The concept of the roller probe has also been utilized for multi-pass welding [19,25]. The probe was composed of a water-filled heat-resistant rotary tyre (1.1 MRayl) withstanding temperatures up to 350° C. However, to improve the design to achieve increased coupling pressure of the probe on a non-planar surface of the as-built WAAM component, the liquid filler material was replaced by a heat-resistant solid core (delay line) made of Polyetherimide Polymer (3.1 MRayl). This modification ensured that I) the probe is fully compliant with the components surface variations at force, II) maximum possible ultrasonic energy is transmitted into the component, and III) signal losses caused by lack of contact with curved WAAM laterals are avoided.

The development of this roller-probe has created an additional ultrasonic challenge. Since the acoustic wave generated by the array on the WAAM roller-probe should traverse two structural mediums with different acoustic properties (*i.e.* the solid delay line and the deformable rubber tyre), the ultrasonic wave refracts at two interfaces both the delay-line/tyre and the tyre/WAAM interfaces to enter the component.

To overcome these challenges during the inspection, the Full Matrix Capture (FMC) data acquisition was deployed. Where, for the N number of elements, raw data is stored in form of a full
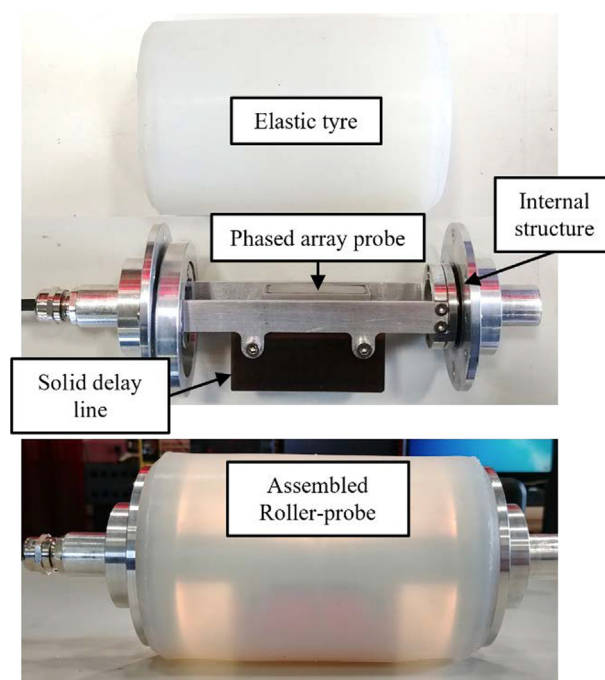

Fig. 1. A complex titanium WAAM component built using oscillation deposition strategy [3] on a substrate plate.

Fig. 2. WAAM Roller-Probe and its constituent components.

time-domain matrix of N^2 A-scans, with each representing an amplitude time sequence [26].

Subsequently, the refraction challenge was solved by ultrasound Delay-and-Sum (DAS) post-processing algorithms called Total Focusing Method (TFM) & Synthetic Aperture Focusing Technique (SAFT) [27,28].

The SAFT algorithm reconstructs the curved profile of a WAAM as-built surface using ultrasound imaging and measures the changes to the rubber interface thickness caused by the force applied to the component. This stage was adopted from a previous investigation of SAFT immersion imaging applied for elementary shape reconstruction [29]. The successfully reconstructed surface is then utilized to compute the adaptive TFM image of the WAAM interior. For this purpose, the algorithm performs a high accuracy raytracing from the transducer's exciting elements toward the pixel through the three mediums and back to the receiving elements. The algorithm performance was assessed where it formed a fully focused image of the WAAM interior and demonstrated successful detection of lack of fusion defects with size 5 × 0.5 × 0.5 (width (X-axis of TFM frame), height (Y-axis of TFM frame), length (along the scan and dimensions obtained from X-ray computed tomography images) - axis) mm [26,30].

Despite the aforementioned benefits of TFM imaging, the required FMC dataset that should be acquired for this imaging method can suffer from the following downsides:

- The FMC data size is typically composed of A-scans for every possible combination of transmitting and receiving elements, resulting in a large single 3-D array. For example, the FMC data acquired using a 64-element array has 4096 a-scans.
- Furthermore, the acquisition rate is also negatively affected, which may not be suitable considering the inspection of a large component at speed, where hundreds of data frames must be stored along with the scan. This limitation may force lower scanning speeds and may result in bottlenecks being introduced from NDE into the overall build process.
- Additionally, the typical element pitch in an array transducer may be only a fraction of a millimeter, therefore the signal strength and the energy are often low in the inherent single element excitation. This may be a limiting factor when inspecting through a number of refractive and attenuative layers such as those found within the roller-probe.

The desire to overcome these challenges drives the investigation of advanced acquisition methods. In this body of work, the authors investigate the benefit of one such technique, called the Virtual Source Aperture (VSA) technique with a combination of the SAFT-TFM package. The goal is to I) enhance the signal strength through increasing the transmitted wave energy that enters the internal volume of the additive components, II) reduce the total data size, and III) increase the maximum acquisition speed, all while maintaining a similar Signal to Noise Ratio (SNR) as compared to conventional FMC data acquisition and subsequent TFM imaging.

Such utilization of phased array technology was first introduced in medicine [31], however, the term VSA for NDE was then invented by [32], and extended for ultrasound imaging through refractive boundary [33]. The technique has since been also adopted and optimized for immersion inspection of complex components [34–36]. A significant reduction in the number of transmissions to match the SNR of FMC-based imaging was achieved when deploying a 32-element sub-aperture.

Furthermore, an accurate surface mapping, with an error lower than 0.1 mm to the true surface, was demonstrated [34,35]. Accurate surface reconstruction has great significance for a precise focal

law calculation and optimal coverage of the signal within the specimen [34,35,37].

The key strength of the VSA technique is that the data is acquired by firing larger element groups or, sub-apertures, increasing the insonification energy within the test piece. This can play a significant role when considering the wave propagation through the attenuative tyre and the delay line of the roller-probe.

In the VSA technique, the beam profile is formed from a virtual point behind the array. Typically, the point is placed above the centre of the sub-aperture with a height equal to the distance from the first element to the centre of the sub-aperture [31]. The sub-aperture is then excited by applying individual delays to its element within forming the desired beam profile. The transmitted wavefront from each sub-aperture reflects from any acoustic impedance discontinuities and is received by the entire array aperture, resulting in a matrix of A-scans similar to convectional FMC, but significantly smaller in size. Subsequently, the TFM image is computed using the VSA data through the DAS approach in the same manner as applied to FMC data with the difference that the transmit locations corresponding to the centre of transmitting sub-apertures are used for the raytracing computations.

In this work, the SAFT-TFM imaging was adapted for processing of the alternative VSA acquisition technique and the applicability of the new approach was investigated via simulation of dry-coupled roller-probe inspection of WAAM with subsequent experimental verification on a custom-designed reference WAAM block with Side Drilled Hole defects (SDH). These cylindrical SDH reflectors are best suited for simulation of inclusions such as keyholes of lack of fusion defects [23], and the use of SDH also enables the establishment of calibration procedures or evaluation of novel inspection techniques.

Moreover, the performance of the technique was evaluated on an inspection through an as-built WAAM surface, also with SDH reflectors, where at first the ability to reconstruct a WAAM interface is analyzed by comparison to a reference optical scan of the specimen and the reconstruction using a classical FMC acquisition. This is followed by a comparative analysis of VSA-TFM and FMC-TFM techniques on WAAM interior imaging capabilities and performances.

Finally, the advantages of the technique are summarized and demonstrated on a mock roller-probe WAAM inspection application.

2. Virtual source aperture technique (VSA-TFM)

2.1. VSA data acquisition

In the VSA technique, the phased array transducer elements are excited in groups with transmission delay laws creating a Virtual Source (VS) above the actual physical aperture. In this work, the virtual point has defined the radius of the arc for the wavefront, as seen in Fig. 3.

Since the VS was a simulated position of the center of the arc from which the beam profile was created, the actual transmission happened by delaying the individual elements in the firing sub-aperture. This delay can be calculated by subtracting the vertical path (h) from the path to each element within the sub-aperture. Therefore, these delays are given by:

$$d_{vsp} = \frac{d}{v_1} = \frac{\sqrt{(x_{rx} - x_v)^2 + y_v{}^2} - h}{v_1} \qquad (1)$$

Where the d_{vsp} is the delay value calculated for each firing element of the sub-aperture, h is the arc radius from which the delays were calculated, v_1 is the velocity of the first medium where the
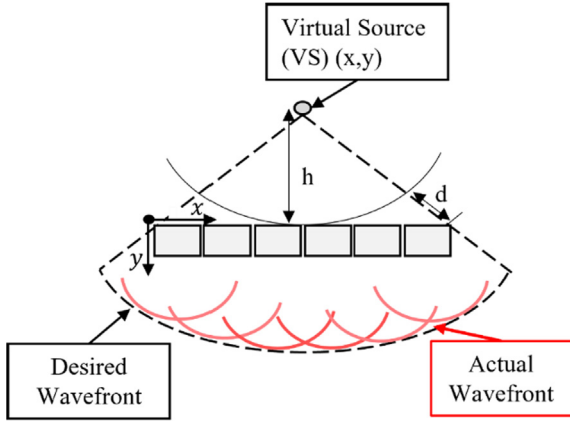
Fig. 3. Diagram illustrating how the virtual source transmission is created by applying delays to the elements of a sub-aperture of 6.

wave propagates, and x_{rx} x_v and y_v are the x coordinates of the firing element and virtual source, and y coordinate of the virtual source, respectively. Once the delays are calculated for the first sub-aperture, they can also be used for the subsequent sub-apertures. This is because the same beam profile is retained as the sub-aperture is shifted across the full aperture of the array by 1 element increments.

2.2. VSA – Total focusing technique

Following the data acquisition, the imaging was accomplished using a TFM algorithm optimized for focusing through three media. To this end, the time of flight (ToF) $(T_{(Tv)})$ from the virtual source (x_v, y_v) towards the pixel (x_p, y_p) with consideration of the refraction at two interfaces (x_{i1}, y_{i1}) and (x_{i2}, y_{i2}), as also illustrated in Fig. 4, were calculated through:

$$T_{(Tv)} = \frac{\sqrt{(x_i - x_v)^2 + (y_i - y_v)^2}}{v_1} + \frac{\sqrt{(x_{i2} - x_i)^2 + (y_{i2} - y_i)^2}}{v_2} + \frac{\sqrt{(x_p - x_{i2})^2 + (y_p - y_{i2})^2}}{v_3} \quad (2)$$

And the ToF $(T_{(R)})$ for the return journey from the pixel to a single receiving element was given by:

$$T_{(R)} = \frac{\sqrt{(x_{i1} - x_r)^2 + (y_{i1} - y_r)^2}}{v_1} + \frac{\sqrt{(x_{i2} - x_{i1})^2 + (y_{i2} - y_{i1})^2}}{v_2} + \frac{\sqrt{(x_p - x_{i2})^2 + (y_p - y_{i2})^2}}{v_3} \quad (3)$$

Given the transmit and receive ToFs calculated through Equations (2) and (3), the signal intensity at a pixel $A(P_{VSA})$ resulting from all transmit-receive combinations can be expressed as:

$$A(P_{VSA}) = \sum_{i=1}^{N_V} \sum_{j=1}^{N_e} R_{i,j}\left(T_{T_V(i)} + T_{R(j)} - \frac{h}{v_1}\right) \quad (4)$$

Where $A(P_{VSA})$ is the pixel amplitude summed from signals $R_{i,j}$, for every transmit-receive combination. The signals were selected according to a timestamp calculated as a sum of the two journeys between I) VS sub-aperture to pixel $(T_{Tv(i)})$ and II) pixel to receive element $(T_{R(j)})$. Since the wave was generated by the physical transducer sub-aperture and not the hypothetical VS position above the aperture, it was important to subtract the ToF for the height (h) from the calculated ToF within the first medium.

The refraction occurring at the interfaces, as illustrated in Fig. 4, was obtained using Snell's law where the refraction angle θ_r was derived from the angle of incidence θ_i and velocities $v_{1,2}$ as follows:

$$\sin\theta_r = \frac{\sin\theta_i}{v_1} * v_2 \quad (3)$$

And further details of the ray tracing algorithm can be found in [28].

Additionally, the quadrature technique was utilized [38,39] to compute the image envelope; hence, improving the final image quality. Consequently, two real and imaginary images were produced from the raw VSA A-scan dataset, and then, were integrated to build the enveloped image. The first image (i.e. the real part) was $(I_{(k,l)})$, with a point index (k, l), and $(I'_{(k,l)})$ is the second image (i.e. the imaginary part) obtained through a Hilbert transform of the raw VSA data set. Therefore, the final image with the envelope feature $I_{envelope}$ could be computed through:
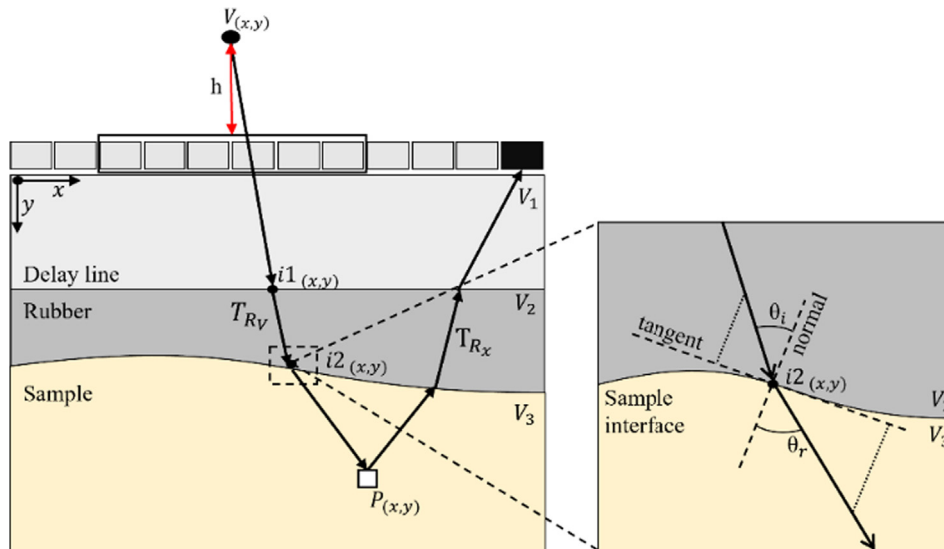

Fig. 4. Diagram illustrating a raytracing for ToF calculations between a virtual source transmitting sub-aperture, a target pixel, and a receiving element. The ray tracing is carried out through three media noting the refractions on planar (delay-line/tyre) and non-planar (tyre/WAAM) interfaces.

$$I_{envelope} = \sqrt{(I_{(k,l)})^2 + (I'_{(k,l)})^2} \tag{5}$$

This approach applied to TFM imaging opened the possibility to compute the frames using a coarser pixel grid size. The results are images that are obtained at a faster pace, but without the loss of signal intensity as compared to simpler TFM variations [39].

Finally, all the images in this work were presented on the dB scale, thus the image values I_{amp_norm} were normalized values obtained from the logarithmic function (6) where the image amplitude I_{amp} was divided by the maximum amplitude found in the image I_{amp_max}.

$$I_{amp\_norm} = 20 \times log_{10} \left(\frac{I_{amp}}{I_{amp\_max}} \right) \tag{6}$$

2.3. Ultrasound surface profile reconstruction (VSA-SAFT)

The roller-probe was dry-coupled to the as-built, commonly irregular, the surface of the WAAM upper surface at some additional applied force for better coupling quality. This introduced some variability in the rubber thickness and its adaptation to the curvature as the force changes. Therefore, these changes must be measured to ensure that the surface profile is accounted for and that more accurate focusing is achieved for the interior image of WAAM.

The soft rubber tyre takes the shape of the WAAM surface profile under applied pressure. On that account, the region within the rubber must be imaged to reconstruct the profile of the tyre/ WAAM interface and the WAAM surface contour. To do so, a dual-medium (i.e., delay line and Tyre) algorithm that was originally developed for FMC-SAFT imaging [27] was adapted to process the VSA data. A dual-medium DAS SAFT algorithm with angular aperture limit can be expressed by:

$$A_{rubber}(P) = \sum_{i=1}^{N_V} \sum_{j_{min}}^{j_{max}} R_{i,j} \left(T_{R_V(i)} + T_{R(j)} - \frac{h}{v_1} \right) \tag{7}$$

where the receive sub-aperture was limited by predefined ranging from an angle $j_{min} = -\alpha$ to angle $j_{max} = \alpha$ to obtain an amplitude response to the pixel $A_{rubber}(P)$ from a total number of N virtual source excitations (V). This restriction of the contributing receive
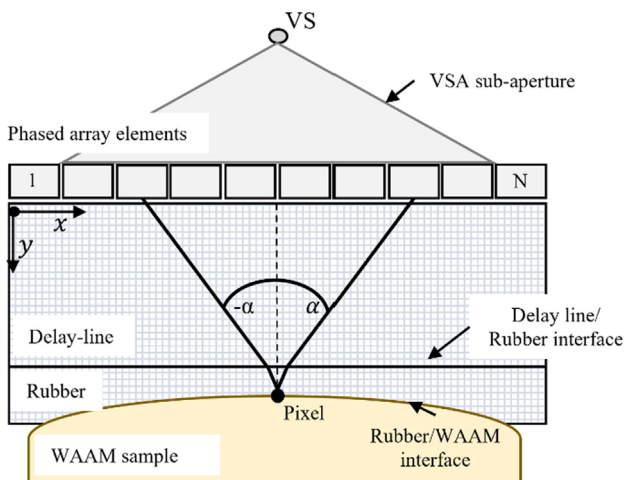

Fig. 5. Diagram illustrating the phased array elements contributing to the pixel of the SAFT image targeting the tyre/WAAM interface and limited by the angle range of -α to..α

elements was illustrated in Fig. 5. The ToFs ($T_{Tv/R}$) were calculated in the coordinate system (x, y) using a velocity of the first v_1 and second medium v_2 and was given by:

$$T_{(Tv)} = \frac{\sqrt{(x_{i1} - x_v)^2 + (y_{i1} - y_v)^2}}{v_1} + \frac{\sqrt{(x_p - x_p)^2 + (y_p - y_{i1})^2}}{v_2} \tag{8}$$

$$T_{(R)} = \frac{\sqrt{(x_{i1} - x_t)^2 + (y_{i1} - y_t)^2}}{v_1} + \frac{\sqrt{(x_p - x_{i1})^2 + (y_p - y_{i1})^2}}{v_2} \tag{9}$$

Where the x_{i1}, x_v, x_p x_t and y_{i1} y_v, y_p, y_t are the x and y coordinates of the virtual source, interception location at the 1st interface, the pixel's location and the receiving element, respectively.

2.4. Ultrasonic-driven WAAM surface profile extraction

Based on the VSA-SAFT surface image, the global thresholding-based algorithm was used to extract Tyre/WAAM interface points [27]. The algorithm was designed to sweep through the image column-by-column while selecting points with the highest signal amplitudes respecting the predefined acceptance/rejection criterion, which in work was set as the minimum amplitude threshold. In the rare cases where two instances of maximum signal amplitudes were observed within a single image column, the algorithm selects pixels located closer to the array as also in practice, the interface was expected to be closer to the array. The algorithm was also designed to skip the columns not containing any pixels that match the acceptance criteria. The curve obtained from this selection process, representing the WAAM contour, was smoothed using polynomial regression to avoid spikes and stored as a 4th polynomial order curve.

2.5. Full matric capture-based imaging

In this work, the FMC-TFM was formed by the summation of the signals at each pixel A(P_{FMC}) from every combination of transmitting and receiving elements. Therefore, the algorithm was given by:

$$A(P_{FMC}) = \sum_{i=1}^{N} \sum_{j=1}^{N} R_{i,j} \left(T_{T(i)} + T_{R(j)} \right) \tag{10}$$

The ultrasonic wave was emitted by a single element and received by all the array elements, while propagating through three media towards the pixel. Therefore, Equation 3 was used to calculate the ToF for both T_T and T_R.

The same methodology presented in [27] was also applied for FMC-based surface profile extraction, to solve refraction at interfaces and to form a final image.

3. Experimental method

3.1. Reference test specimen

For the initial stage, a custom-designed WAAM calibration sample (Block A), shown in Fig. 6, was chosen for the model-based and experimental work presented in this paper.

Ti-6Al-4 V (Ti-64) Block A was built using a plasma arc deposition process with a parallel deposition strategy [40] where 3 straight beads were deposited next to each other in the same direction. The deposition process parameters are summarized in Table 1. The molten pool formed beneath the deposition torch was protected from oxidation using a local shielding device continuously supplying argon gas onto the hot titanium at a rate of 110 l/minute. Even and odd layers of the components were deposited in opposite
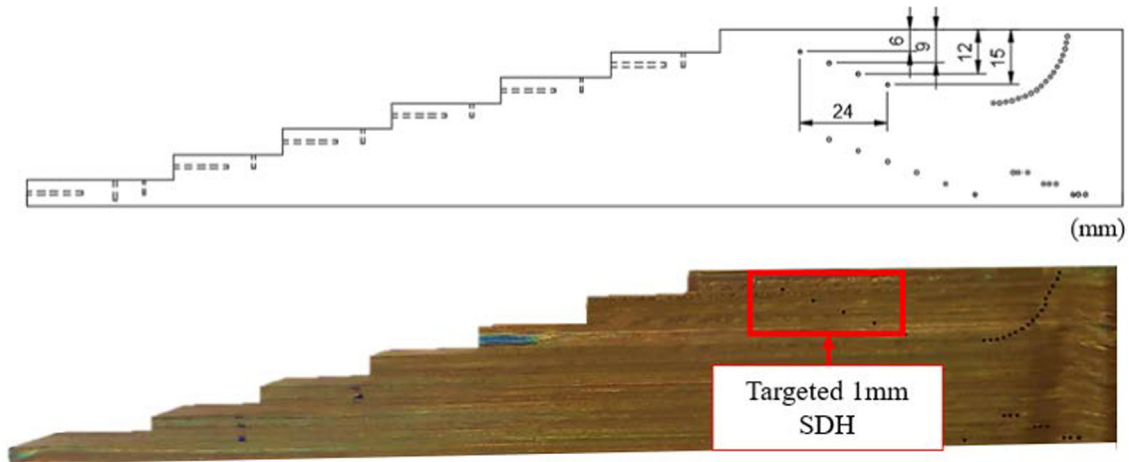
Fig. 6. Calibration titanium WAAM block (Block A).

Table 1
Deposition Parameters of Reference Test Specimen.

Region	Current [Amps]	Travel speed (mm/s)	Wire feed speed (m/min)
Outer 2 beads	180.0	3.6	2.3
Core bead	180.0	3.6	2.0

directions to prevent the material from being overbuilt forming bumps at the start edge.

Once the component was completely deposited, a step-shaped section, depicted in Fig. 6, was machined out of the WAAM. The inspection was carried out by phased array ultrasound testing to assure no substantial defects were present in Block A.

Subsequently, reference reflectors in the shape of flat bottom holes, intended for other studies, and a wide depth range of Side Drilled Holes (SDH) of 1.0 mm in diameter were introduced using an electro-discharge-machining process.

The SDH defects, marked in the red rectangle (Fig. 6), were used to evaluate the performance of the VSA throughout the simulation and experimental work. These 4 selected SDHs vary in depth, ranging between 6.0 and 15.0 mm, with a 6.0 mm spacing between them.

3.2. Simulation of the virtual source aperture versus full matrix capture

Initially, a simulation was conducted to compare the quality of images constructed from the VSA data and the FMC-based ones. The simulation was conducted in the CIVA (EXTENDE, 2020) software application which has proven effective for modelling and validating ultrasonic inspection results in various scenarios [41,42]. The inspection parameters such as delay line, rubber thickness and PAUT were chosen to be identical to the planned experimental roller-probe inspection scenario. The roller-probe was modelled as a phased array transducer placed on a 26 mm thick delay line and a 6 mm thick rubber interface as seen in Fig. 7. The defects selected for the simulation corresponded to the SDH defects presented in Block A in section 3.1 and marked in Fig. 6. To minimize discrepancies between the real and simulated material properties, the velocity and the attenuation properties of different components were considered in the model. These values were obtained through a pulse-echo measurement of the individual components of the roller-probe, including the delay line and the rubber, and the titanium WAAM test specimen at the frequency of 5 MHz in a direc-
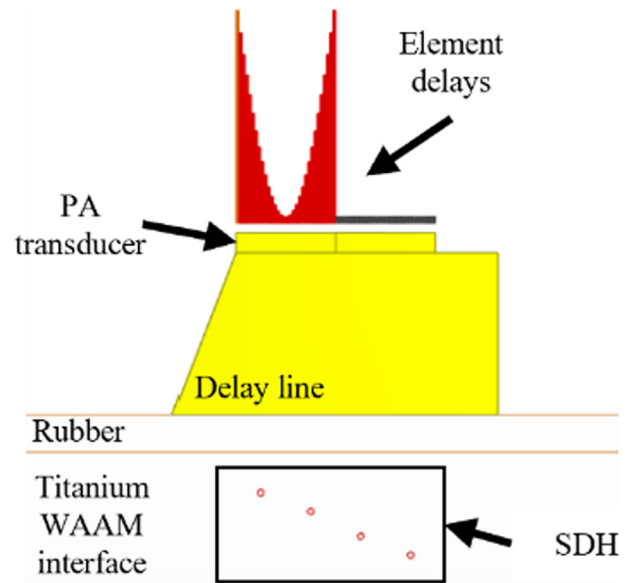

Fig. 7. Simulation setup in the CIVA interface.

tion matching the inspection scenario. Table 2 summarizes the measured values used in the simulation. The ultrasonic wave interactions with all interfaces and reflectors were enabled in the model for the most accurate simulation of the real-world inspection scenario despite the computational expenses caused by this.

A MATLAB script was generated to calculate delays for individual elements within the VSA sub-aperture, according to Equation 1 explained in Section 2.1., and then the delays were imported into the CIVA as the VSA beamforming is not integrated by default within CIVA. The velocities were assigned to different domains according to the measured values presented in Table 2. Elements were excited at a frequency of 5 MHz with a Hanning signal and 50% bandwidth at −6 dB. A sampling frequency of 50 MHz was

Table 2
Attenuation data.

Material	Attenuation (dB/mm)	Acoustic velocity (m/s)
Delay line	0.5	2480
Rubber	1.9	1006
Calibration WAAM	0.09	6300

used for the acquisition. Once the simulation was completed, the raw data matrix was exported and processed in MATLAB (R2021a) using the algorithms developed and explained in Sections 2.1 and 2.3.

3.3. Experimental inspection hardware setup

The ultrasonic roller-probe, used during the experiments, was based on a 5 MHz 64-element linear array with specifications presented in Table 3. The array was enclosed in a rotary tyre and acoustically coupled to a solid delay line, which line was used as a central core of the roller-probe transmitting the ultrasound wave from the array transducer into the coupling tyre. The acoustic velocities for the delay line and rubber are seen in Table 2. To achieve a smooth frictionless rolling of the roller-probe, a liquid coupling gel was used to fill the roller-probe.

The ultrasound roller-probe was mounted on a KUKA KR-90 robot allowing for precise delivery and positioning of the sensor on the WAAM component for data collection. A Force/Torque sensor (FTN-GAMMA-IP65 SI-130–10, Schunk, max. z-axis force 130 N) was employed to connect the roller-probe to the robot as seen on Fig. 8. The sensor was interfaced with the rest of the robotic control package [19] for continuous force/torque measurement and real-time adjustments to the robot pose for keeping a constant applied force on the component. Provided that, a steady force of 100 N was applied to the WAAM specimen during the inspection. The data were acquired using an LTPA array controller (PEAK NDT, Derby UK) mounted on the robotic arm itself.

3.4. Experimental data acquisition and processing

The 16-bit FMC and VSA data were acquired with a sampling frequency of 50 MHz. The excitation voltage was set to 200 V and the duration of the excitation pulse was 100 ns. All data was recorded with a receiver hardware gain of 50 dB.

The VSA sub-aperture used throughout the experiment was kept constant at 32 elements with an increment of 1 element forming a total of 33 firings per set of VSA data. The size of the sub-aperture used in this work was found to be the best performing configuration as indicated by [34,35]. With the 33 sub-apertures transmitting and all elements receiving, a total of 64 × 33 A-scans were stored, each containing 3000 samples. The number of samples was enough for each A-scan to reach below the expected imaging window. The FMC data used for comparison was acquired using a full aperture of 64 elements, thus, forming a matrix of 64 × 64 A-scans, each 3000 samples long.

The SAFT surface identification was formed on an image with 10 pixels per image mm, therefore, a pixel grid size of 320 × 30 pixels. The TFM images were formed using 6 pixels per/mm where the adaptive TFM image was formed as a grid with the size of 132 × 156 pixels and images formed for the calibration (machined) sample were set to a grid of 192 × 72 pixels.
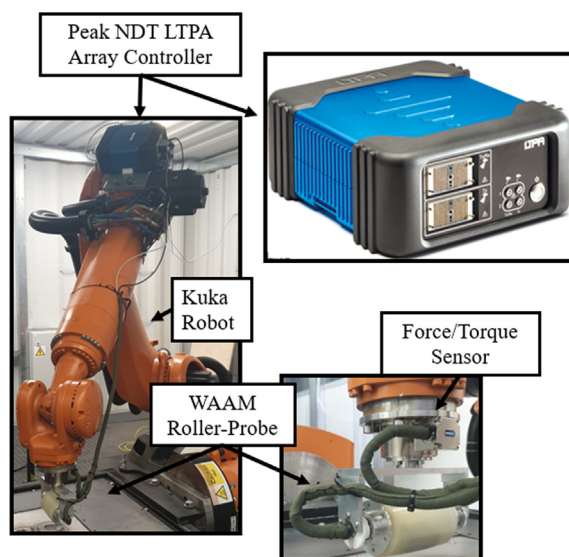
Table 3
PAUT parameters.

Array Parameters	Value
Element Count	64
Element Pitch	0.5 mm
Element Elevation	10 mm
Element Spacing	0.1 mm
Centre Frequency	5 MHz
Element Material	1 – 3 Piezocomposite
Manufacturer	Imasonic (France)

Fig. 8. Experimental setup showing a KUKA robot, array controller and the WAAM roller-probe.

4. Results and discussion

4.1. Evaluation of VSA on a calibration titanium WAAM sample through a machined surface using a modelling approach and experiment

First, the application of the VSA was investigated via SDH defects inspection modelling through the machined surface of the Block A. Fig. 9 (a, b) show the results of the inspection simulation based on the FMC and VSA datasets, respectively. Each image was plotted on a −20 dB scale with respect to the image maximum value.

Clear indications for four 1.0 mm SDH reflectors could be observed in both model-based images of Fig. 9 (a, b). The VSA-TFM image was plotted after normalizing it with respect to the maximum of the FMC-TFM image. The results showed an increased maximum signal amplitude by up to 2.3 dB observed for the VSA image where 33 excitations of the 32 element sub-aperture were taken place.

The same approach to normalizing and scaling the images was applied to the experimental inspection images seen in Fig. 9 (c, d). Similar to the simulation case, the experimental VSA-TFM image showed an increase of up to 1.8 dB in the maximum amplitude as compared to the FMC-TFM. However, this increase was accompanied by a higher noise level in the near-surface region. The near-surface noise was not present in the simulation results as the noise could only be introduced at the imaging stage as speckle noise in CIVA and not in the form of scattering A-scan noise on the FMC & VSA raw data. Provided that the imaging process was carried out in MATLAB 2020a and did not have the possibility of introducing the noise to FMC and VSA raw data, the simulation images were formed noise-free.

Furthermore, comparing the SDH defect amplitudes obtained from VSA and FMC data, Fig. 10 (a, b) display 2 plots where the maximum image intensities in dB along the vertical axis in the simulation and experiment are extracted, respectively. There was a good agreement between the maximum amplitudes of the two plots corresponding to simulations and experiments. The difference between retrieved peak amplitudes, from all SDH, by FMC-TFM and VSA-TFM, are summarized in Table 4. The values in the Table confirmed the energy strength retrieved from the reflectors
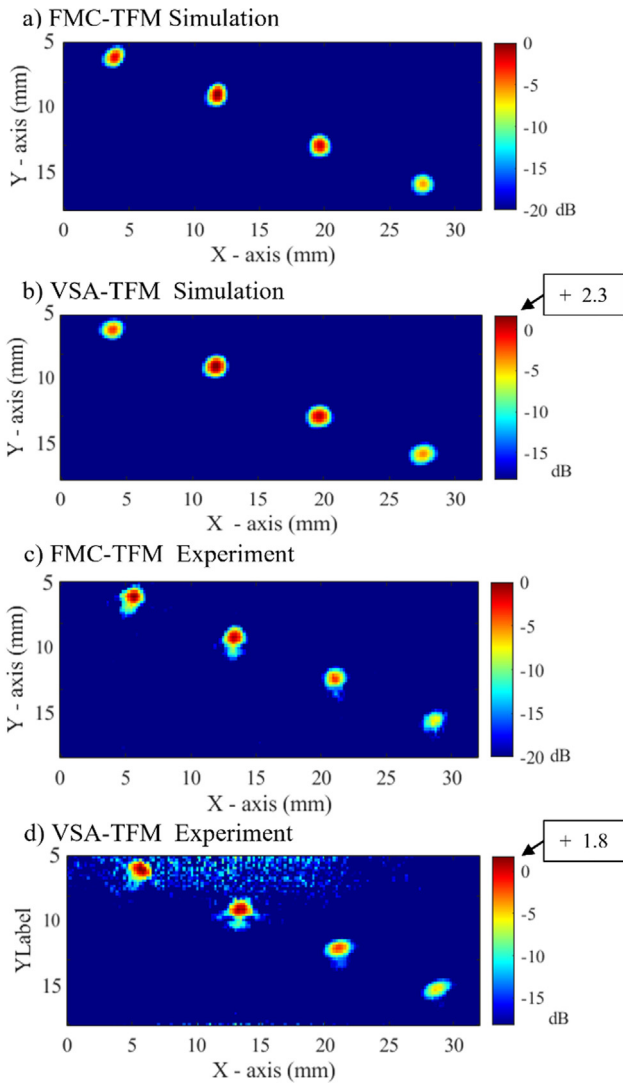
Fig. 9. TFM imaging results based on the simulated (a) FMC and (b) VSA data sets as well as experimental (c) FMC, and (d) VSA data.

Fig. 10. Plots showing maximum vertical intensities of the defects in VSA-TFM and FMC-TFM images obtained through (a) simulation and (b) experiment.

was higher by up to 2.5 dB in the simulation and 2.7 dB in the experiment when using the VSA aperture. The lowest amplitude increase was achieved for the near-surface SDH of only 0.8 dB for simulation and 1.8 dB in the experiment while the same increase was observed for the 12 mm deep defect. In general, the maximum amplitude levels and the amplitude differences observed between the VSA and FMC plots in the simulation were consistent for all four defects and correlate well to the VSA and FMC experimental amplitude discrepancies.
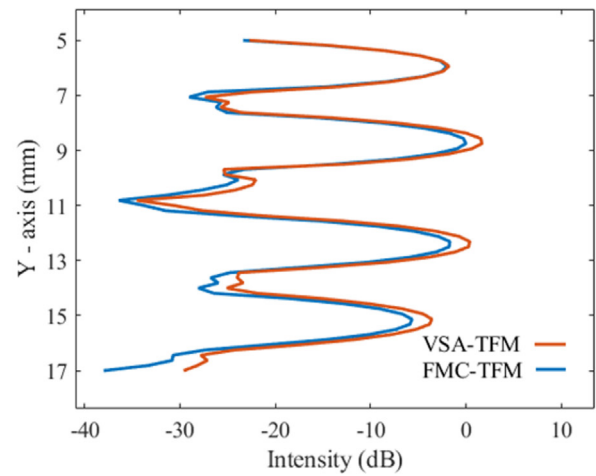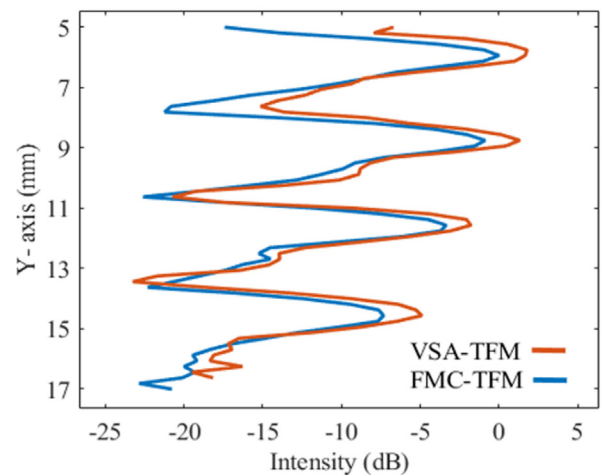
Moreover, a similar SNR of approximately 20 dB was achieved by both FMC and VSA-based imaging approaches, which complimented the goals of this work. As can be seen from Fig. 10, the noise baseline for the simulations was lower which is the result of noise-free raw data used in the imaging.

4.2. Evaluation of VSA on WAAM inspection through as-built surface

4.2.1. As-built WAAM sample

After successful verification of the proposed VSA technique on inspection through the machined surface, the experiments were also carried out through an as-built surface of a manufactured Ti-64 WAAM wall (Block B).

Block B, depicted in Fig. 11, was built using a plasma arc WAAM process, where each layer approximately 35 mm wide was deposited by a single oscillating bead [43]. Five layers were deposited to the height of approximately 15 mm for this component.

The evaluation of the VSA technique was conducted by inspection of Block B containing three SDH defects with 1.0 mm in diameter. The holes were drilled approximately 20 mm deep into the sample while each SDH was placed directly 5 mm below the peak of the surface contour.

4.2.2. Investigation of virtual source aperture data for surface reconstruction

In this section, the application of VSA data for ultrasound surface reconstruction was evaluated. The results were compared with the FMC-SAFT surface reconstruction approach and a true surface of the WAAM obtained via a non-contact metrology laser scan, performed using a laser profiler with a vertical accuracy of 12 μm [44].

The SAFT angle limitation that was applied to FMC-SAFT, as described in the background section 2.2.1, was set to -α = ±7.5° as reported in [27]. These limits were changed for the receiving elements of the VSA-SAFT to ± 5°, where tighter limits were found

Table 4
Signal strength of individual SDH in the Block A.

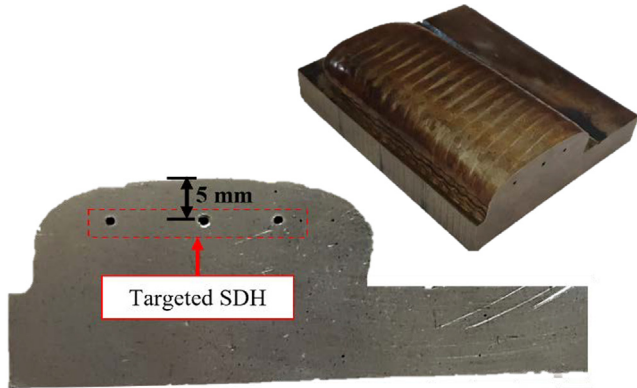| DefectDepth (mm)	FMC-Modelling (dB)	VSA Modelling (dB)	FMC Experiment (dB)	VSA Experiment (dB)
6.0	− 0.7	0.1	0	+ 1.8
9.0	0	+ 2.3	− 0.9	+ 1.3
12.0	−3.5	+ 0.9	− 3.5	− 1.7
15.0	−9.1	−6.4	− 7.3	− 4.8

Fig. 11. Titanium WAAM sample with 1 mm SDH used for experimental work through the as-built surface.

to perform more accurately. The surface finding amplitude threshold was found to adequately filter noise when set to −10 dB from the maximum, for FMC-SAFT and −15 dB for VSA-SAFT. The surface images were plotted in a 0 to −30 dB scale where the features are best represented with the noise largely omitted in the image.

Pixels with the highest amplitude were identified in each column of the image as a point representing the surface profile as can be seen in Fig. 12. A curve was fitted through the pixels with maximum amplitudes in each FMC-SAFT and VSA-SAFT image representing the non-planar WAAM upper surface. There are also two distinct indications from the tyre/air interface at the two corners of the tyre/WAAM interface where the contact with the WAAM surface ends. These indications are stronger in amplitude due to the larger impedance mismatch of rubber and air; hence easily identifiable. In light of this, the part of the curve contained between

these two corner indications can be readily extracted and used for WAAM interior TFM imaging in the later sections.

Comparing the two profiles reconstructed by FMC-SAFT and VSA-SAFT to a laser reference scan, a strong agreement between the 3 curves was observed in Fig. 13 (a).

However, to accurately measure the deviation (error) $\Delta_{average}$ of the FMC-SAFT and VSA-SAFT estimated surfaces with reference to the true surface, the estimation error for each of the two techniques can be calculated through:

$$\Delta_{average} = \frac{1}{p} \sum_{p=1}^{p=n} |S_{Opt}^p - S_{UT}^p| \tag{10}$$

Where the S_{Opt}^p and S_{UT}^p are the y-axis surface points obtained by the laser and the ultrasound technique, respectively, and n (n = 300) is the total number of points p. The comparison was only made on the segment of the surface where both curves coexisted.

Fig. 13 (b) shows an error distribution along the X-axis when comparing the curve to the true surface. By averaging the error between a VSA-SAFT to the true surface using Equation 10, the $\Delta_{average}$ was calculated to be 0.0481 mm while the FMC-SAFT showed a slightly lower $\Delta_{average}$ of 0.042 mm.

However, in both cases, the average error was less than a quarter of the wavelength (λ = 0.2 mm) in the second (rubber) medium at the selected frequency. This was a crucial finding as an error value larger than a quarter of the wavelength could have a detrimental effect on the final TFM image summation causing a phase difference larger than π/2 [34].

4.2.3. Evaluation of the VSA-TFM imaging on the as-built WAAM component with 1 mm SDH defects.

After the successful surface profile detection, they were factored in the TFM algorithm to form the fully focused interior
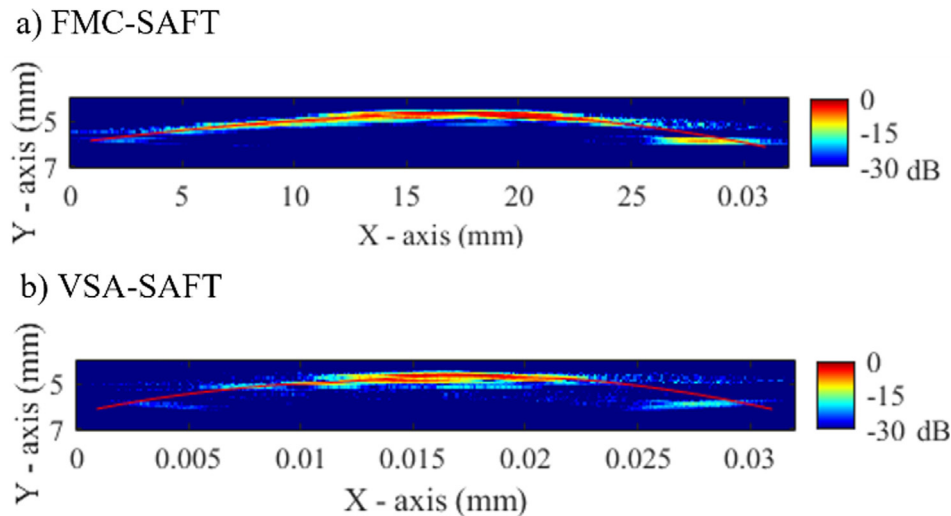

Fig. 12. Surface reconstruction images: (a) FMC-SAFT and (b) VSA-SAFT.

a)

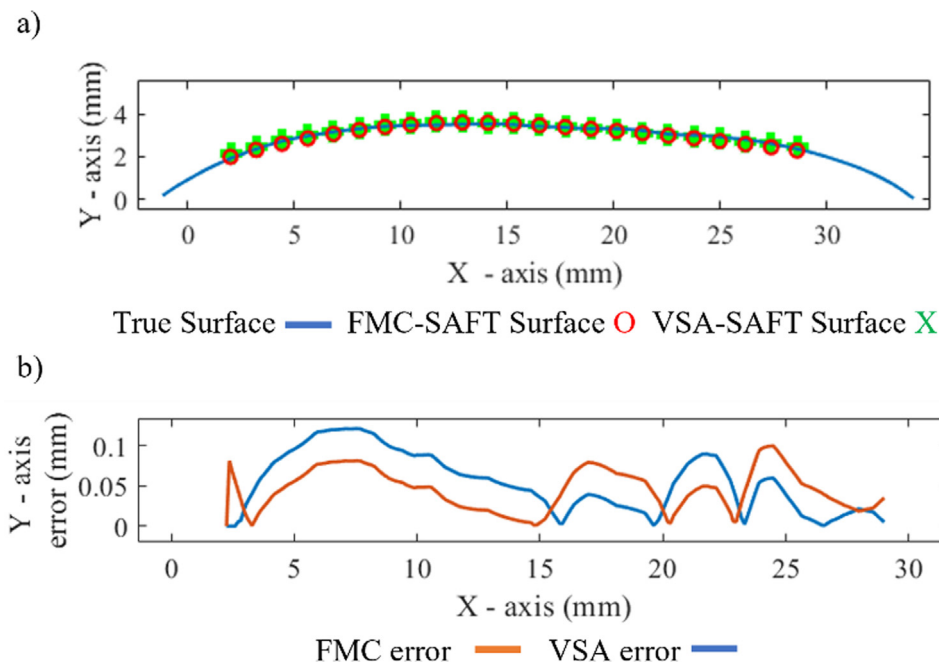True Surface ▬▬ FMC-SAFT Surface ○ VSA-SAFT Surface ✕

b)

Fig. 13. Assessing the surface reconstruction accuracy of VSA-SAFT and FMC-SAFT as compared to the optical scan results.

WAAM images through both VSA-TFM and FMC-TFM as illustrated in Fig. 14 (a, b), respectively. The FMC-TFM and VSA-TFM were normalized to the maximum of the VSA-TFM signal corresponding to a centre SDH reflector. Both images were presented on a dB scale ranging between the maximum amplitude of the centre reflector and −20 dB of this amplitude. This enabled focusing the analysis on the signal retrieved from the SDH reflectors rather than a subsurface noise level present in the images. Since the maximum signal intensity from the subsurface noise was found stronger than the amplitude of the centre SDH, in both images, a large portion of the surface signal was seen saturated due to its presence above the dB scale threshold.

The reference FMC-TFM, showed clear indications from the three SDHs, with a peak amplitude at −4.7 dB, however, the SDH on the right-hand side of the image had a weaker signal amplitude, at −9.1 dB, as compared to the rest of them. The VSA-TFM image was presented in Fig. 14 (a). All three defects were detectable in the image with comparably equal strength, ranging between −4.8 dB and −7.5 dB, from all three reflectors. However, the subsurface noise was stronger as well, which was the result of increased UT beam energy in the VSA and thus the stronger reflections at the tyre/WAAM interface.

Following the visual analysis of the images, Fig. 15 was plotted to show the signal intensity map of the SDH defects along the horizontal axis created from a region 4 mm beneath the surface reflections to the depth of a baseplate interface (15 mm below the surface). To analyze and compare the signal strength retrieved from this region, the FMC-TFM plot was renormalized to a maximum of the defect region in VSA-TFM. This facilitated the comparison of the signal strength retrieved from all the SDH defects to the detected peak.

A balanced SNR of approximately 18 dB was achieved for the defects located at the center and left in the FMC-TFM image while the defect on the right-hand side showed an SNR of around 15 dB. A similar level of SNR at approximately 20 dB for the centre defect and 18 dB for the left-hand side defect was observed in the VSA-TFM image, however, in contrast to the previous case, the defect on the right also displayed the SNR level of 18 dB. Table 5 shows the signal levels of SDHs in both VSA and FMC based TFM images

where higher peak signals were achieved in the VSA-TFM by 2.55 dB, 4.69 dB and 6.42 dB for left, center and right SDHs, respectively. It is worth noting, that the naturally occurring material noise levels have increased as well without negatively affecting the SNR.

Additionally, the images in Fig. 14 displayed a back wall echo of Block B and a near-wall reflection that creates a characteristic dead zone limiting the detectability of defects near the surface. A stronger surface signal zone was visible in the VSA-TFM image reaching approximately 3.5 mm, while for the FMC-TFM image this area produces less interference for the defect signals as it shrinks to around 2 mm in depth and mostly concentrates in the corners.

4.3. Benefits of the VSA-TFM imaging for inspection automation

Once ultrasound arrays were considered for automated inspections, one should be aware of the data frame rates as these can dictate the inspection speed. The maximum theoretical frame rate is constrained by the acquisition time, which is given by the number of excitations (sub-apertures), the time it takes for the ultrasonic wave to propagate through the 3 media (2 media inside the roller-probe + inspected WAAM) or a time of the wave decay below to a sufficiently low level. Since the material properties, and hence, the wave propagation time of flights is constant, the number of excitations and receptions can be reduced to increase the frame rate. Therefore, employing the VSA acquisition offers a significant advantage over the conventional FMC data acquisition owing to the reduced number of excitations required in the VSA. During the experimental work, the acquisition speed of the VSA was observed to be almost twice the speed of the FMC data acquisition. Furthermore, the VSA frame data size of 13.3 MB had seen a reduction of almost 37% in the TFM frame size of 21.3 MB. The data in this work were stored in.mat file format.

In this paper, the data was acquired using a program developed within the LabVIEW environment. During the experiment, the frame rates of 3.1 Hz and 1.6 Hz were achieved by the VSA and the FMC, respectively. Therefore, in an example WAAM wall inspection scenario where the sample is 2 m long and post-deposition robotic inspection is carried out using a stable scanning
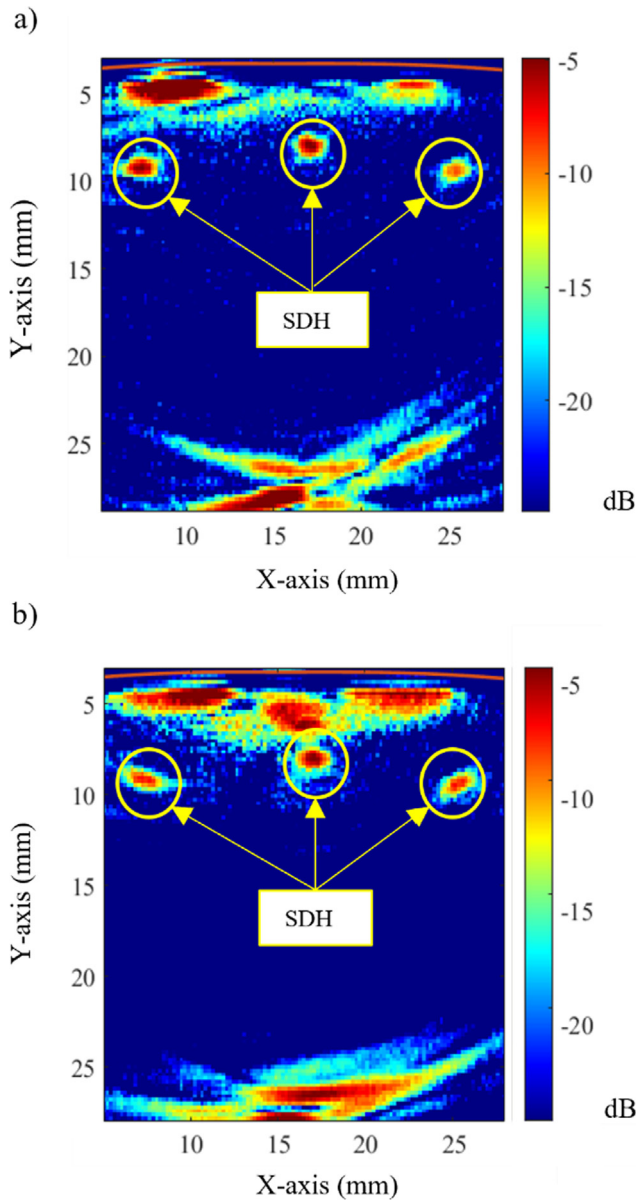
a)

b)

Fig. 14. (a) VSA-TFM and (b) FMC-TFM images capturing the interior of the Block B with 3 SDHs.
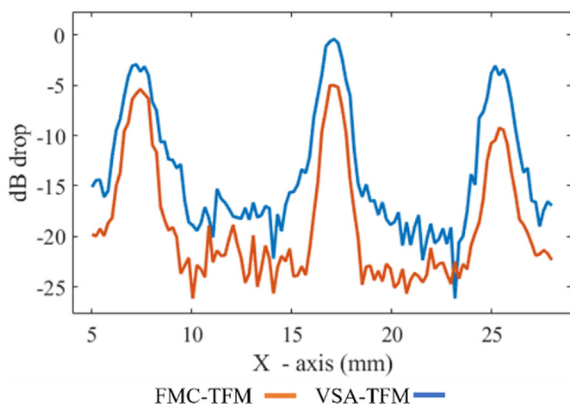

Fig. 15. Plot showing the maximum horizontal intensity of the SDH defects indications in VSA-TFM (blue) and FMC-TFM (orange) images.

Table 5
Signal strength of the SDHs in Block B.

Defect position	FMC Experiment (dB)	VSA Experiment (dB)
left	−5.06	−2.51
centre	−4.69	0
right	− 9.12	−2.7

speed of 10 mm/s, the VSA technique would enable the system to collect almost twice as the number of frames as collected by the FMC during the inspection, summarized in Table 6. This also implied that an increased frame density could be achieved through VSA while using the same scan speed, which is critical in terms of enhancing the detection probability.

To realize the largest inspection increment size (resolution) required during an automated scan and yet sufficiently fine to not skip/lose any subsurface defects, a simulation, presented in Fig. 16, was conducted to show the width of the ultrasound beam transmitted into the WAAM. The beam width was measured using the 6 dB drop method [45] from the maximum beam amplitude to be 8.4 mm for the roller-probe configuration during the inspection of titanium WAAM (simulation parameters explained in section 4.2). This focal width indicated the longest allowable distance between two consecutive frames that would have still provided full coverage of the WAAM interior with an ultrasound beam during the robotic scan. To maintain a frame density of approximately 4 mm, considering a sufficient overlap, Table 7 showed a possibility to double the inspection speed as compared to FMC data acquisition, where the inspection speed would be also significantly reduced to almost a half as well. This improvement reaching close to 50% in scanning speed could result in a significantly reduced time of inspection and therefore, simplified NDT integration into the built process.

The imaging stage was integrated and implemented in MATLAB 2020a. The processing time was evaluated on setup with two Intel Xeon 6482R processors with a clock speed of 3 GHz and 192 GB of Random-Access Memory. The elapsed time for the SAFT algorithm to estimate the surface contour was 1.8 s since the focal laws were pre-loaded into the system. The full adaptive TFM algorithm for both VSA-TFM and FMC-TFM was measured to be 131 s. Since the complex ray-path searching calculations were computed using MATLAB and were not optimized for speed using advanced programing on for example GPU, the speed of the image computation was not of concern for this work.

5. Conclusions & Future work

5.1. Conclusions

This paper presents an adaptation and deployment of a raw data acquisition called virtual source aperture technique, evaluated with a post-processing algorithm package based on SAFT surface reconstruction and three-layer adaptive TFM imaging for a dry coupled roller-probe inspection of as-built WAAM components.

The applicability of the VSA was first evaluated by simulation and experimental validation of a typical inspection performed on a custom-designed Ti-64 calibration WAAM block. The comparison

Table 6
Comparison of inspection parameters achieved by VSA and FMC.

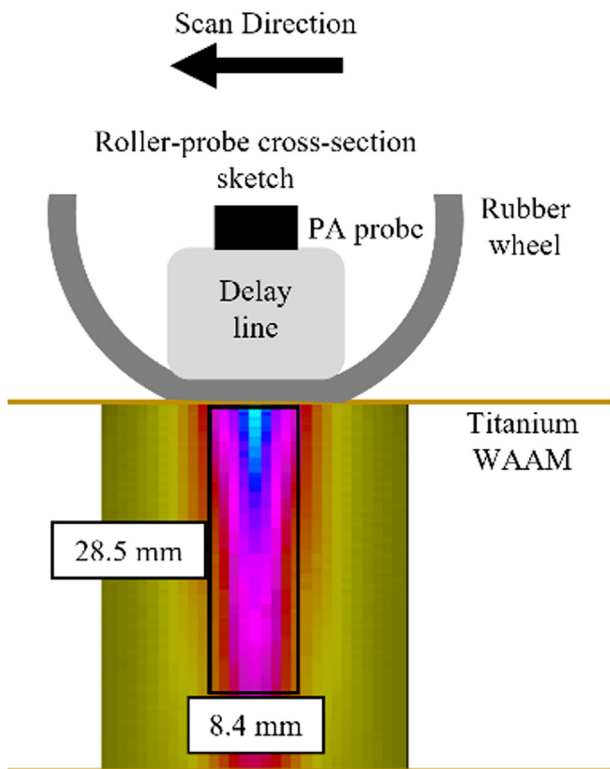| Method	Frames/ WAAM at 10 mm/s	Frames/ mm
VSA	620	6.2
FMC	320	3.2

Fig. 16. Simulation of the beam profile in inspection travel direction, providing information about a beam coverage.

Table 7
Comparison of inspection parameters achieved by VSA and FMC.

Method	Max. scanning speed (mm/s)	Time of Inspection (seconds)
VSA	12.4	161.3
FMC	6.4	312.5

of simulation and experiment confirmed the increase in energy levels enabled by VSA to be at least 0.8 dB and 1.5 dB respectively within the WAAM component with comparable SNR levels.

Furthermore, the experimental mock inspection of an as-built WAAM sample through its non-planar surface was conducted to demonstrate the potential to reconstruct the surface using VSA and subsequently, compute a precise interior image of the wall. The experimental work was conducted on a WAAM wall with three 1.0 mm SDH reflectors.

During the inspection, an accurate VSA-SAFT surface estimation was obtained, in a close match to FMC-SAFT-based reconstruction. Comparing the derived surface profile with that measured by a laser scanner demonstrated an accuracy better than the required threshold of $\lambda/4$.

Using an obtained surface profile, the interior image was computed, showing successfully detected SDH defects with an increased signal strength of up to 6.42 dB as compared to the FMC-based TFM image. While comparable overall SNR levels were achieved, the VSA-TFM image achieved significantly higher SNR for the defect on the right of the center as compared to its FMC counterpart.

Lastly, it can be concluded that the VSA in combination with the SAFT-TFM imaging package offers the potential to reduce the data size by 37.5 %, due to a markedly lower number of transmissions, while also increasing the potential inspection speed by 48% when compared to the previously reported FMC-TFM approach. While

the imaging performance is similar, the advantage of the speed and data size reduction can simplify the integration of the inspection during the build process.

5.2. Future work

Future work includes integration of the approach to a WAAM manufacturing environment and evaluating the performance of the VSA on in-process inspection of WAAM components, built using various deposition strategies and materials and at speed. Additionally, research work involves the evaluation of the technique for inspection of naturally occurring defects such as delamination, crack, keyholes, or lack of fusion or porosity. This would be conducted in various WAAM scenarios and it may include curtailing the roller-probe's geometrical configuration (including PAUT) according to the research needs. Further, the authors aim to investigate the application of the technique on samples at elevated temperatures and develop compensation algorithms accordingly. Lastly, the authors aim to optimize the algorithms for fast image processing to fully enable the advantages provided by the VSA technique.

Declaration of Competing Interest

The authors declare that they have no known competing financial interests or personal relationships that could have appeared to influence the work reported in this paper.

Acknowledgments

References

[1] T. Hauser, R.T. Reisch, S. Seebauer, A. Parasar, T. Kamps, R. Casati, J. Volpp, A.F. H. Kaplan, Multi-Material Wire Arc Additive Manufacturing of low and high alloyed aluminium alloys with in-situ material analysis, J. Manuf. Processes 69 (2021) 378–390.

[2] S.W. Williams, F. Martina, A.C. Addison, J. Ding, G. Pardal, P. Colegrove, Wire+ arc additive manufacturing, Mater. Sci. Technol. 32 (7) (2016) 641–647.

[3] E. Aldalur, F. Veiga, A. Suárez, J. Bilbao, A. Lamikiz, High deposition wire arc additive manufacturing of mild steel: Strategies and heat input effect on microstructure and mechanical properties, J. Manuf. Processes 58 (2020) 615–626.

[4] J. Hönnige et al., Residual stress and texture control in Ti-6Al-4V wire+ arc additively manufactured intersections by stress relief and rolling, Mater. Des. 150 (2018) 193–205.

[5] X.i. Chen, F. Kong, Y. Fu, X. Zhao, R. Li, G. Wang, H. Zhang, A review on wire-arc additive manufacturing: typical defects, detection approaches, and multisensor data fusion-based model, The International Journal of Advanced Manufacturing Technology 117 (3-4) (2021) 707–727.

[6] B. Wu, Z. Pan, D. Ding, D. Cuiuri, H. Li, J. Xu, J. Norrish, A review of the wire arc additive manufacturing of metals: properties, defects and quality improvement, J. Manuf. Processes 35 (2018) 127–139.

[7] P. Cawley, Non-destructive testing—current capabilities and future directions, Proceedings of the Institution of Mechanical Engineers, Part L: Journal of Materials: Design and Applications 215 (4) (2001) 213–223.

[8] J. Mireles, S. Ridwan, P.A. Morton, A. Hinojos, R.B. Wicker, Analysis and correction of defects within parts fabricated using powder bed fusion technology, Surf. Topogr. Metrol. Prop. 3 (3) (2015) 034002, https://doi.org/10.1088/2051-672X/3/3/034002.

[9] J. García-Martín, J. Gómez-Gil, E. Vázquez-Sánchez, Non-destructive techniques based on eddy current testing, Sensors 11 (3) (2011) 2525–2565.

[10] Lopez, A., et al. Mapping of non-destructive techniques for inspection of wire and arc additive manufacturing. in Proceedings of the 7th International Conference on Mechanics and Materials in Design, Portugal. 2017.

[11] J. Tomlinson, A. Wagg, and M, Whittle, Ultrasonic inspection of austenitic welds, 1980.

[12] E. Mohseni et al., Ultrasonic phased array inspection of wire plus arc additive manufactured (WAAM) titanium samples, in *58th Annual British Conference on Non-Destructive Testing*, 2019.

[13] A. Lopez, R. Bacelar, I. Pires, T.G. Santos, J.P. Sousa, L. Quintino, Non-destructive testing application of radiography and ultrasound for wire and arc additive manufacturing, Addit. Manuf. 21 (2018) 298–306.

[14] Y. Javadi et al., Ultrasonic phased array inspection of a Wire+ Arc Additive Manufactured (WAAM) sample with intentionally embedded defects, Addit. Manuf. 29 (2019) 100806.

[15] J.K. Na, J.L. Blackshire, S. Kuhr, Design, fabrication, and characterization of single-element interdigital transducers for NDT applications, Sens. Actuators, A 148 (2) (2008) 359–365.

[16] B.W. Drinkwater, P.D. Wilcox, Ultrasonic arrays for non-destructive evaluation: A review, NDT and E Int. 39 (7) (2006) 525–541.

[17] J.H. Kurz, A. Jüngert, S. Dugan, G. Dobmann, C. Boller, Reliability considerations of NDT by probability of detection (POD) determination using ultrasound phased array, Eng. Fail. Anal. 35 (2013) 609–617.

[18] N.a. Xu, Z. Zhou, Numerical simulation and experiment for inspection of corner-shaped components using ultrasonic phased array, NDT and E Int. 63 (2014) 28–34.

[19] M. Vasilev, C.N. MacLeod, C. Loukas, Y. Javadi, R.K.W. Vithanage, D. Lines, E. Mohseni, S.G. Pierce, A. Gachagan, Sensor-enabled multi-robot system for automated welding and in-process ultrasonic NDE, Sensors 21 (15) (2021) 5077, https://doi.org/10.3390/s21155077.

[20] Y. Javadi et al., In-process inspection of multi-pass robotic welding. Review of Progress in Quantitative Nondestructive, Evaluation (2019).

[21] Y. Javadi, E. Mohseni, C.N. MacLeod, D. Lines, M. Vasilev, C. Mineo, E. Foster, S.G. Pierce, A. Gachagan, Continuous monitoring of an intentionally-manufactured crack using an automated welding and in-process inspection system, Mater. Des. 191 (2020) 108655, https://doi.org/10.1016/j.matdes.2020.108655.

[22] Javadi, Y., et al. Intentional weld defect process: from manufacturing by robotic welding machine to inspection using TFM phased array. in AIP Conference Proceedings. 2019. AIP Publishing LLC.

[23] E. Mohseni et al., Model-assisted ultrasonic calibration using intentionally embedded defects for in-process weld inspection, Mater. Des. 198 (2021) 109330.

[24] E. Mohseni et al., A high temperature phased array ultrasonic roller probe designed for dry-coupled in-process inspection of wire+ arc additive manufacturing, 47th Annual Review of Progress in Quantitative Nondestructive Evaluation, 2020.

[25] R.K.W. Vithanage, E. Mohseni, Z. Qiu, C. MacLeod, Y. Javadi, N. Sweeney, G. Pierce, A. Gachagan, A phased array ultrasound roller probe for automated in-process/interpass inspection of multipass welds, IEEE Trans. Ind. Electron. 68 (12) (2021) 12781–12790.

[26] C. Holmes, B.W. Drinkwater, P.D. Wilcox, Post-processing of the full matrix of ultrasonic array data for non-destructive evaluation, NDT and E Int. 38 (8) (2005) 701–711.

[27] R. Zimermann, E. Mohseni, D. Lines, R.K.W. Vithanage, C.N. MacLeod, S.G. Pierce, A. Gachagan, Y. Javadi, S. Williams, J. Ding, Multi-Layer Ultrasonic Imaging of As-Built Wire + Arc Additive Manufactured Components, Addit. Manuf. 48 (2021) 102398, https://doi.org/10.1016/j.addma.2021.102398.

[28] R. Zimermann et al., Implementation of an ultrasonic total focusing method for inspection of unmachined wire+ arc additive manufacturing components through multiple interfaces, 47th Annual Review of Progress in Quantitative Nondestructive Evaluation, 2020.

[29] W. Kerr, S.G. Pierce, P. Rowe, Investigation of synthetic aperture methods in ultrasound surface imaging using elementary surface types, Ultrasonics 72 (2016) 165–176.

[30] C. Holmes, B. Drinkwater, P. Wilcox, The post-processing of ultrasonic array data using the total focusing method, Insight-Non-Destructive Testing and Condition Monitoring 46 (11) (2004) 677–680.

[31] C.H. Frazier, W.D. O'Brien, Synthetic aperture techniques with a virtual source element, IEEE Trans. Ultrason. Ferroelectr. Freq. Control 45 (1) (1998) 196–207.

[32] M. Sutcliffe, P. Charlton, M. Weston, Multiple virtual source aperture imaging for non-destructive testing, Insight-Non-Destructive Testing and Condition Monitoring 56 (2) (2014) 75–81.

[33] M. Sutcliffe, M. Weston, P. Charlton, B. Dutton, K. Donne, Virtual source aperture imaging for non-destructive testing, Insight-Non-Destructive Testing and Condition Monitoring 54 (7) (2012) 371–379.

[34] E. Hoyle, M. Sutcliffe, P. Charlton, J. Rees, Virtual source aperture imaging with auto-focusing of unknown complex geometry through dual layered media, NDT and E Int. 98 (2018) 55–62.

[35] E. Hoyle et al., Virtual Source Aperture with Real Time Focussing of Known Geometry Through Dual Layered Media, in BINDT 56th Annual Conference 3B5 (freely available on Researchgate), 2017.

[36] J. Camacho, J.F. Cruza, Auto-focused virtual source imaging with arbitrarily shaped interfaces, IEEE Trans. Ultrason. Ferroelectr. Freq. Control 62 (11) (2015) 1944–1956.

[37] R.E. Malkin, A.C. Franklin, R.L.T. Bevan, H. Kikura, B.W. Drinkwater, Surface reconstruction accuracy using ultrasonic arrays: Application to non-destructive testing, NDT and E Int. 96 (2018) 26–34.

[38] D. Lines et al., Modelling of echo amplitude fidelity for transducer bandwidth and TFM pixel resolution, in 47th Annual Review of Progress in Quantitative Nondestructive Evaluation, 2020.

[39] Nicolas Badeau, G.P.-A., Alain Le Duff. Use of the Total Focusing Method with the Envelope Feature. 30 March 2020 [accessed 9 April 2020]; Available from: https://www.olympus-ims.com/en/resources/white-papers/use-of-the-total-focusing-method-with-the-envelope-feature/.

[40] X. Xu et al., Preliminary investigation of building strategies of maraging steel bulk material using wire+ arc additive manufacture, J. Mater. Eng. Perform. 28 (2) (2019) 594–600.

[41] Dubois, p., et al., Simulation of Ultrasonic, Eddy Current and Radiographic Techniques within the CIVA Software Platform, in 10th European Conference on Non-Destructive Testing, 2010.

[42] F. Foucher, P. Dubois, Applications and recent evolutions of the CIVA Simulation Platform, in 18th World Conference on Nondestructive Testing, 2012.

[43] A. Paolini, S. Kollmannsberger, E. Rank, Additive manufacturing in construction: a review on processes, applications, and digital planning methods, Addit. Manuf. 30 (2019) (2019) 100894.

[44] Compact laser scanner for automation & robotics, cited 2021 11/02 Available from: https://www.micro-epsilon.co.uk/2D_3D/laser-scanner/scanCONTROL-2600/, 2021.

[45] X. Wang et al., Three-dimensional damage quantification of low velocity impact damage in thin composite plates using phased-array ultrasound, Ultrasonics 110 (2021) 106264.